Magnetic Property Calibration of Low-Permeability Materials for Vibrating Sample Magnetometers Using Neural Networks

Xiaohan Kong[1], Yuji Uehara[2], Naoya Terauchi[3], Natsuko Sato[3], Yoshibumi Matsuda[3], Masanori Nagano[3], Hajime Igarashi[1]

[1]Graduate School of Information Science and Technology, Hokkaido University, Sapporo, Japan
[2]Magnetic Device Laboratory Ltd., Kawasaki, Japan
[3]TAIYO YUDEN CO., LTD. Takasaki, Japan

This paper proposes a new method to calibrate the *B-H* properties measured by the vibrating sample magnetometer (VSM) for bar-shaped samples. It compensates for finite size and demagnetization effects using the neural networks (NNs) trained based on finite element analysis. Once the NNs are trained, they provide fast prediction of calibration results. The results from the proposed method are compared with those from the capacitive cancellation method, regarded as a reference due to its immunity to the effects of the demagnetizing field.

***Index Terms*—Vibrating sample magnetometer, magnetic property, finite element method, neural network**

I. Introduction

The soft magnetic composites (SMC), composed of insulated iron particles, have been widely used in electric machines and devices. SMC has the advantage that it does not easily become magnetically saturated compared to ferrite. The vibrating sample magnetometer (VSM) [1], capable of operating at high field strengths, is ideal for evaluating the magnetic properties of SMC materials. The VSM directly measures the magnetic moment (M) under the effect of diamagnetic field in response to the applied magnetic field strength (H_a). There are two calibration steps: the first step corrects for finite size effects, and the second step compensates for the demagnetizing field.

In the first step, the finite size effect is compensated to obtain the accurate M-H_a curve. The standard VSM measurement suggests using cube-shaped samples with edge lengths under 3 mm to meet the point dipole assumption. Unfortunately, cubes are not suitable for SMC measurements because the large demagnetizing field inside a cube makes it difficult to saturate. In contrast, a bar-shaped sample is easier to reach saturation. However, the approximation of a point dipole source is no longer valid in such situation, which can introduce errors of up to 20% [2]. The manufacturers of the VSM devices suggest that each measurement should be calibrated using pure nickel sample shaped identically to the tested bar-shaped sample. However, this requirement might be difficult to implement in practice. For this reason, we need a more generalized calibration method for the finite size effect.

In the second step, the M-H_a curve is calibrated to obtain the inherent B-H properties, excluding demagnetization effects. Analytical methods [3-6] for approximate values of demagnetization factor N have been proposed. However, these methods usually only consider sample geometry and ignore the dependence of N on B-H characteristics. In fact, Chen et al. [7] and Bahl [8] prove that even for identical sample geometries, N varies depending on the B-H characteristics. Since the magnetic properties of the material are unknown in practical measurements, it is not accurate to perform the calibration solely using analytical solutions. In [9], an iterative process based on magnetic field analysis using finite element method (FEM) is proposed to predict N, providing better calibration results. However, the iterative processes may suffer from slow convergence and sensitivity to initial conditions. A more straightforward prediction method is needed to make it more accessible to engineers.

This study proposes a fast method for calibrating magnetic properties without iterative processes, where the calibration factors relevant to the finite size effect and demagnetization are evaluated using the neural network (NN). We restrict ourselves here to low-frequency magnetic properties up to a few hundred kHz, where eddy currents can be neglected. Our method relies on prior knowledge of the permeability and geometry range of the sample material. Extensive FEM calculations are then performed to train the NNs. Once trained, the NNs can be used to quickly calibrate samples within this range. Careful consideration should be given to the design of the NN architecture to ensure reliable corrections. The results obtained using the proposed method are compared with those from the capacitive cancellation method [10], considered a reference because it is unaffected by the demagnetizing field.

II. Finite Size Effect Calibration

Fig. 1 depicts the procedure of the proposed method.

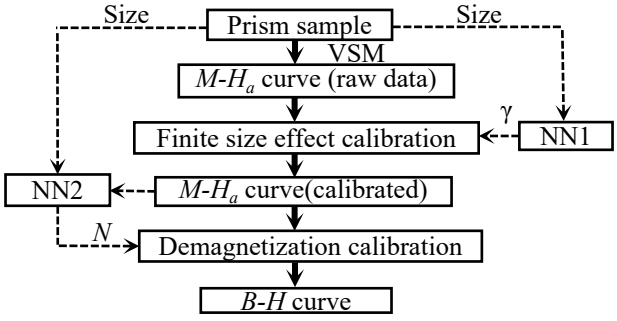

Fig. 1. Proposed calibration process.

This method involves two steps, each predicting a calibration factor (γ and N) through a NN. The calibration for the finite size effect is described below and that for demagnetization is formulated in the next section.

Fig. 2 shows a schematic of the VSM device. The pick-up coil is located close to the test sample to measure the magnetic flux. The electromagnet together with iron yoke maintains a uniform field H_a in the central area.

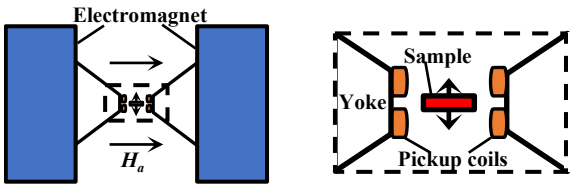

Fig. 2. Schematic diagram of the VSM device.

The sinusoidal motion of the sample generates a time-varying magnetic field in the pick-up coils, which can be approximated using the dipole model as

$$\boldsymbol{B}(r) = \frac{1}{4\pi\mu_0}\left[-\frac{\boldsymbol{J}}{r^3} + \frac{3(\boldsymbol{r}\cdot\boldsymbol{J})\boldsymbol{r}}{r^5}\right], \quad (1)$$

where $\boldsymbol{J}$ is the total magnetic moment of the sample. As shown in Fig. 3 (a), for an infinite small sample with magnetic moment of J_0, the induced voltage $V_0(t)$ in the pick-up coil (x_c, y_c, z_c) can be evaluated by the Faraday law, which is given by

$$V_0(t) = J_0\left(\frac{\Delta Z_0}{\Delta R_0{}^5} - \frac{5\Delta X_0{}^2\Delta Z_0}{\Delta R_0{}^7}\right)\frac{3a\omega NS}{4\pi}\cos(\omega t), \quad (2)$$

where $\Delta X_0, \Delta Z_0, \Delta R_0$ depict the relative position between the sample and coil, a and ω are the vibrating magnitude and angular frequency, respectively, and N and S denote the number of turns and the area of the coil. For a sample with finite size, as shown in Fig. 3(b), the induced voltage is obtained by integrating the voltages produced by all its sub-elements as follows:

$$V_s(t) = \sum_{i=1}^{k} J_i\left(\frac{\Delta Z_i}{\Delta R_i{}^5} - \frac{5\Delta X_i{}^2\Delta Z_i}{\Delta R_i{}^7}\right)\frac{3a\omega NS}{4\pi}\cos(\omega t), \quad (3)$$

where J_i is the magnetic moment of sub-element, and k is the number of sub-elements.

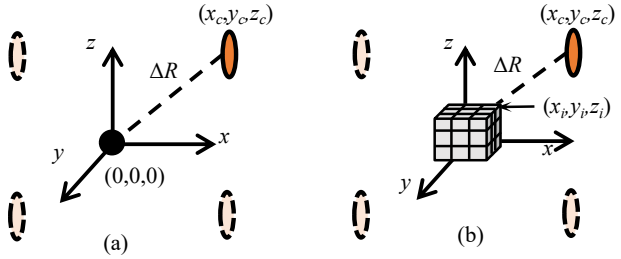

Fig. 3. Equivalent model for calculating induced voltage, (a) infinite small sample, and (b) finite-size sample.

If the samples shown in Fig. 3(a) and (b) have the same total moment, we have

$$J_0 = \sum_{i=1}^{k} J_i. \quad (4)$$

We define the ratio $V_s(t)/V_0(t)$ as the finite-size ratio γ, which is generally greater than 1 and varies with the sample geometry. The VSM manufacturers recommend using pure nickels shaped identically with tested samples to determine γ experimentally. Alternatively, γ can be calculated numerically. The distribution of J_i in the sample under a uniform applied field H_a can be directly obtained from the FEM analysis, and $V_s(t)/V_0(t)$ is then obtained based on equation (2), (3) and (4), as depicted in Fig. 4 (a). Fig. 4(b) displays *B-H* curves for 9 different materials, for each of which we computed the $\gamma(H_a)$ for three different sample geometries. In total, this involved FEM analysis for 27 samples. Fig. 4 (c) shows the profiles of $\gamma(H_a)$ for the three sample geometries, where γ is primarily influenced by the sample geometries and also dependence on *B-H* characteristics. In this study, we neglect the influence of the *B-H* curve for simplicity. The profile of $\gamma(H_a)$ is represented using five equidistant points γ_i (i ranges from 1 to 5) across the range of H_a from 400 to 800,000 A/m. The reason why $\gamma(H_a)$ converges to certain values is that J_i tends to be uniformly distributed as it approaches the saturation region. This suggests that γ can be predicted from the sample geometry.

TABLE I
SIZES OF TEST SAMPLES

Material	SMC-1 ($\mu_r\approx14$)			SMC-2 ($\mu_r\approx16$)		
#	1	2	3	1	2	3
w (mm)	3.01	4.01	5.01	2.98	3.98	4.98
t (mm)	0.51	0.57	0.52	0.48	0.48	0.48
h (mm)	0.56	0.56	0.56	0.50	0.50	0.50
Material	SMC-3 ($\mu_r\approx28$)			SMC-4 ($\mu_r\approx36$)		
#	1	2	3	1	2	3
w (mm)	3.00	4.01	5.00	2.99	3.99	4.98
t (mm)	0.50	0.51	0.51	0.49	0.48	0.49
h (mm)	0.57	0.56	0.57	0.48	0.48	0.48

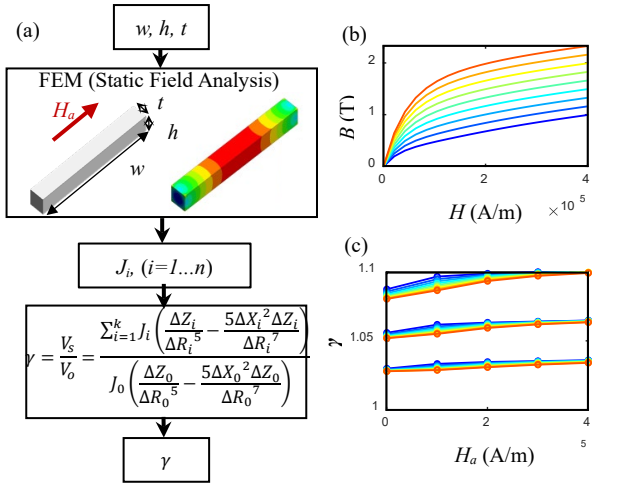

Fig. 4. Finite size effect, (a) calculation process for γ, (b) *B-H* curves for nine different materials, and (c) $\gamma(H_a)$ for three sample geometries with nine different B-H characteristics.

To predict γ_i from the geometrical parameter of the test sample, we introduce NN1 shown in Fig. 5. The input data consists of normalized geometrical parameters, w, t, h and the output is γ_i. As shown in Fig. 5, NN1 consists of three hidden layers with 80 neurons each, following the multilayer

perceptron (MLP) model, and is built on the TensorFlow platform.The training of NN1 is performed over 250 data sets, where the inputs are randomly varied. We performed 600 iterations until convergence.

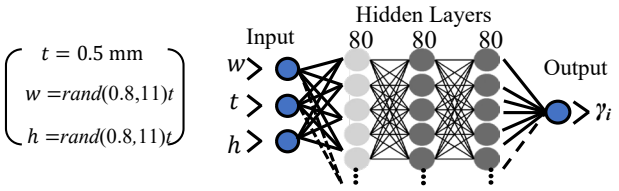

Fig. 5. Structure of NN1 for calibration of finite size effect.

Using this method, we performed calibration for 12 test samples, the sizes of which are listed in TABLE I. These samples are made of four kinds of SMC materials. From SMC-1 to SMC-4, the powder particle size of SMC increases, and the permeability increases correspondingly. Fig. 6 shows the M-H_a curves before and after the calibration using $\gamma_i$predicted by NN1. After calibration, samples with the same material have the same saturation magnetization, which can serve as a criterion for effective calibration.

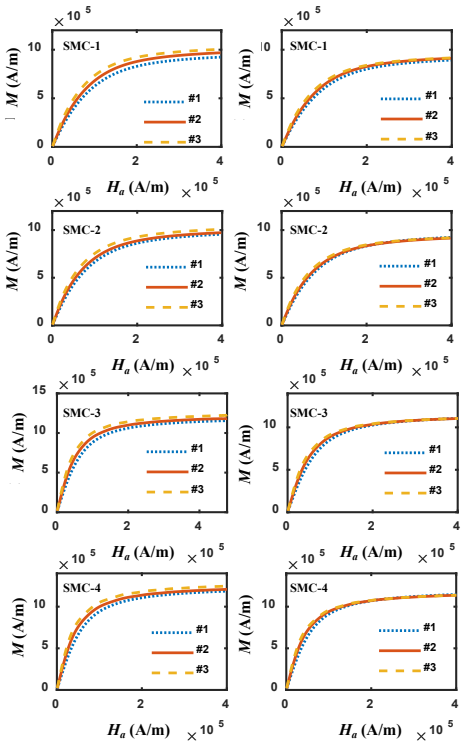

Fig. 6. M-H_a curves before(left) and after(right) calibrated by γ with NN1.

III. Demagnetization Calibration

This section describes the calibration for demagnetization. The effective field H in a bar-shaped sample, illustrated in Fig. 7, is the superposition of the applied field H_a and the demagnetizing field H_d, that is

$$H = H_a - H_d, \tag{4}$$

The M-H_a curve requires further calibration to determine the inherent B-H characteristic. The demagnetizing factor N is used to calculate H_d as follows:

$$H_d = NM, \tag{5}$$

Subsequently, the calibrated B-H characteristic can be obtained from

$$B = \mu_0(H + M). \tag{6}$$

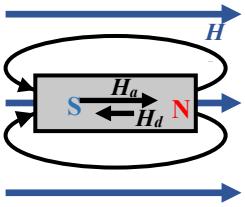

Fig. 7. Demagnetization.

Note that N depends on both sample geometry and magnetic property, particularly the relative permeability μ which is unknown during measurements. What we obtain through measurement is the M-H_a curve. To establish the relationship between the M-H_a curve and N, we solve the inverse problem using a NN rather than the iterative FEM simulations described in [9].

We define χ_a as the ratio of M to H_a obtained from VSM measurements. Generally, the M-H_a curve is nonlinear, resulting in different corresponding χ_a values for different H_a. We trained a NN to predict N values corresponding to various inputs, including different values of χ_a and the shapes of B-H curves. NN2 shown in Fig. 8 is constructed for this target, where sample geometry w, h, t and χ_a are the input data, and N as the output. The training data was built as shown in Fig. 9. Generating random values for w, h, t and relative permeability μ_r, we perform static field FEM analysis, which yields the average field $\langle H\rangle$ and $\langle B\rangle$ over the sample. Then, the average value of M and H_d over volume are obtained from

$$M = \left(\langle B\rangle/\mu_0 - \langle H\rangle\right), \tag{7}$$

and

$$H_d = H_a - \langle H\rangle. \tag{8}$$

Then, the volume-averaged N and χ_a can be determined from

$$N = H_d/M, \tag{9}$$

and

$$\chi_a = dM/dH_a. \tag{10}$$

Though χ_a and N are resulted from the FEM analysis, the former is input to NN2 with w, h, t, the latter is chosen as its output. Similar to NN1, NN2 also follows the MLP model and consists of three hidden layers with 40 neurons each. NN2 was trained on 2,000 data sets with randomly varying inputs, and the training involved 4,000 iterations to achieve convergence.

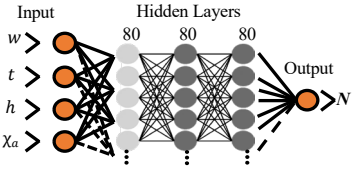

Fig. 8. Structure of NN2 for demagnetization calibration.

The use of NN2 is shown in Fig. 9 (b). Once we determine the sample geometry and measure the M-H_a curve to obtain χ_a, we use NN to evaluate N for each point on the M-H_a curve. Since M is a nonlinear function of H, meaning that using a single N value is inappropriate, we assume different N values for each sampling point on the M-H_a curve, following [11]. We calculate dM/dH_a to get χ_a^k, input it into NN2, and use the resulting N_k for correction of each point.

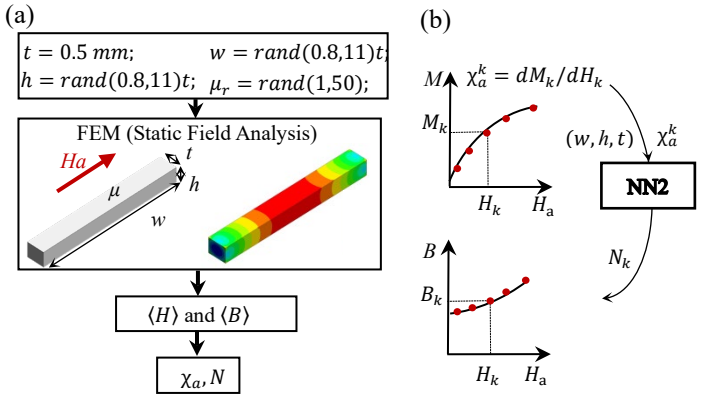

Fig. 9. Training data preparation and prediction method. (a)Training data produced from FEM, and (b) usage of NN2.

Based on NN2, the N values of samples with five different geometries are computed for various χ_a. The results are plotted in Fig. 10 (a). The dependence of N on μ_r is shown in Fig. 10 (b). When μ_r approaches 1, it approaches the values obtained by Aharoni [6]. This indicates that NN2 includes the analytical solution in the limit $\mu_r \rightarrow 1$.

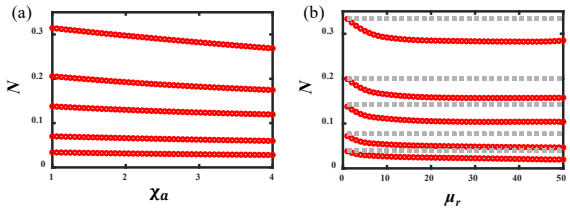

Fig. 10. N values evaluated by NN2, where w= [0.3, 0.6, 1, 2, 3] and h=t=0.5. As w decreases, N increases. (a)N versus χ_a, (b) N versus μ_r.Grey dashed lines show the values obtained from Aharoni's approximation [6].

With the proposed method, the calibration has been carried out for the samples listed in TABLE I. There are two commonly used analytical N values: one is Osborn's approximation for an ellipsoid [3], and the other is Aharoni's approximation for a prism [6]. As shown in Fig. 11, compared to the other two approximations (Osborn's in the left column and Aharoni's in the right column), the proposed method gives the B-H curves closer to the reference data measured by the capacitive cancellation method where low H_a data are available.

To improve the accuracy of the proposed method, it would be effective to consider predicting the γ value based on both the B-H curve and shape for NN1. Although the iterative method can be employed to repeat the first and second steps to eliminate the error caused by neglecting the effects of B-H curves in the first step, this would increase the computing cost. Another possibility is to directly combine the two steps and predict the B-H curve from the M-H_a curve using a single NN.

IV. Conclusion

This paper has presented a new NN-based method for predicting VSM calibration parameters. The well-trained NN enables instant parameter prediction, eliminating the need for FEM calculations or iterative processes, making it accessible to engineers in diverse fields. The structure and weighting coefficients of NNs obtained in this study will be made openly available for use by other researchers.

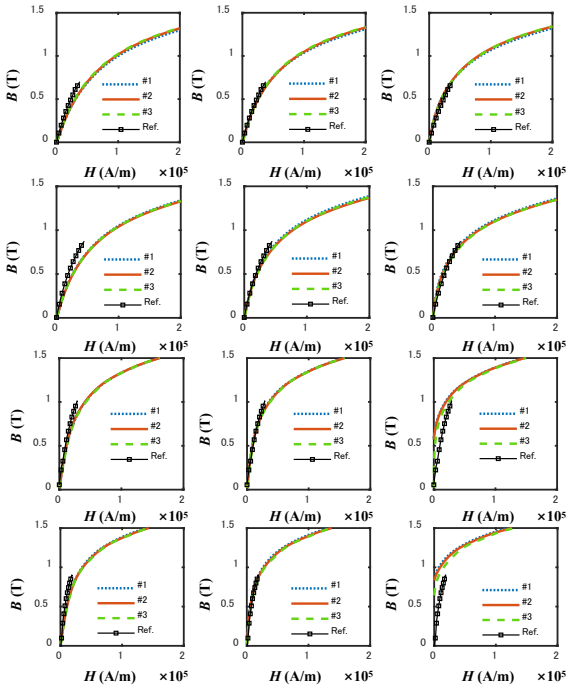

Fig. 11. B-H curves after the calibration using Osborn's(left), proposed(middle) and Aharoni's(right) method. Ref. represents the results measured by the capacitive cancellation method.

References

[1] Simon Foner, "Versatile and Sensitive Vibrating - Sample Magnetometer," Rev Sci Instrum., vol.30, pp. 548-557, July 1959.

[2] J. Lindemuth et al., "Finite sample size effects on the calibration of vibrating sample magnetometer," IEEE Trans. Magn.,vol. 59, pp. 1-5, November 2023.

[3] J. A. Osborn, "Demagnetizing factors of the general ellipsoid," Phys. Rev., vol. 67, pp. 351, June1945.

[4] R.I. Joseph, "Ballistic demagnetizing factor in uniformly magnetized rectangular prisms, " J. Appl. Phys., vol. 38, pp. 2405–2406, June 1967.

[5] D.X. Chen, J.A. Brug and R.B. Goldfarb, "Demagnetizing factors for cylinders," IEEE Trans. Magn., vol. 27, pp. 3601–3619, July 1991.

[6] A. Aharoni, "Demagnetizing factors for rectangular ferromagnetic prisms," J. Appl. Phys., vol. 83, pp. 3432–3434, March 1998.

[7] D.X. Chen, E. Pardo and A. Sanchez, "Demagnetizing factors for rectangular prisms," IEEE Trans. Magn., vol. 41, pp. 2077-2088, June 2005.

[8] C.R.H. Bahl, "Estimating the demagnetization factors for regular permanent magnet pieces," AIP Adv., vol. 11, pp. 075028, July 2021.

[9] K. Etse, X. Mininger. "Determination of Demagnetizing Factors for Various Geometries using an Iterative Numerical Approach," J. Magn. Magn. Mater., vol. 564, pp.170151, December 2022.

[10] Y. Sato et al., "Accuracy Investigation of High-Frequency Core-Loss Measurement for Low-Permeability Magnetic Materials," IEEE Trans. Magn., vol. 59, pp. 1-5, November 2023.

[11] Chen Du-Xing et al., "Demagnetizing correction in fluxmetric measurements of magnetization curves and hysteresis loops of ferromagnetic cylinders," J. Magn. Magn. Mater., vol. 449, pp. 447-454. October, 2018.